Promoting a well-dispersion of MoO$_3$ nanoparticles on fibrous silica catalyst via one-pot synthesis for enhanced photoredox environmental pollutants efficiency

N.M. Izzudin [a], A.A. Jalil [a,b,*], M.W. Ali [a,b], F.F.A. Aziz [a], M.S. Azami [c], N.S. Hassan [a], A.A. Fauzi [a], N. Ibrahim [d], R. Saravanan [e], M.H. Hassim [a]

[a] School of Chemical and Energy Engineering, Faculty of Engineering, Universiti Teknologi Malaysia, 81310 UTM Johor Bahru, Johor, Malaysia
[b] Centre of Hydrogen Energy, Institute of Future Energy, 81310 UTM Johor Bahru, Johor, Malaysia
[c] Faculty of Applied Sciences, Universiti Teknologi MARA Perlis, 02600 Arau, Perlis, Malaysia
[d] Faculty of Civil Engineering Technology, Universiti Malaysia Perlis, 02600, Arau, Perlis, Malaysia
[e] Department of Mechanical Engineering, Universiti of Tarapacá, Avda. General Velasquez, 1775, Arica, Chile

HIGHLIGHTS

- Nanoporous of FSMo was efficaciously synthesized via microemulsion method.
- FSMo catalyst demonstrated a preserved spherical morphology with dendrimeric silica fibre.
- The well-dispersion of Mo element in the FSMo catalyst greatly inhibits the electron-hole recombination.
- FSMo showed the 75% and 69% towards simultaneous remediation of Cr(VI) and TC, respectively.
- h$^+$, .•OH$_{ads}$, and e$^-$ are noted as the reactive species that play significant role in the photoredox of Cr(VI) and TC.

GRAPHICAL ABSTRACT
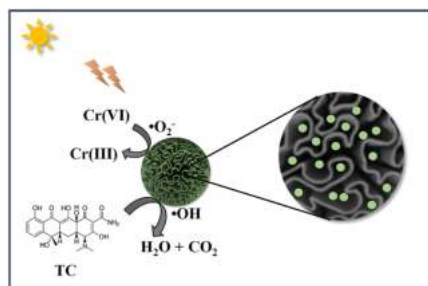
ARTICLE INFO

ABSTRACT

The coexistence of pharmaceutical compounds and heavy metals in the aquatic environment has resulted in complications in the treatment process and thus, causing uproar among the citizens. The radical-based photo-catalysis technology has aroused as an excellent method to eliminate both heavy metal and pharmaceutical compounds in the water. Herein, reported the utilization of the microemulsion technique for the preparation of nanoporous fibrous silica-molybdenum oxide (FSMo) towards simultaneous photocatalytic abatement of hex-avalent chromium (Cr(VI)) and tetracycline (TC). The FESEM analysis showed the spherical morphology of the FSMo catalyst with dendrimeric silica fiber. The synthesized FSMo catalyst exhibited narrowed bandgap, high crystallinity, and well Mo element dispersion for enhanced photo-redox of Cr(VI) and TC. Remarkably, simultaneous remediation of the Cr(VI) and TC over FSMo demonstrated superior photocatalytic efficiency, 69% and 75%, respectively, than in the individual system, possibly due to the effective separation of photoinduced charges. The introduction of the Mo element to the silica framework via microemulsion technique demonstrated better dispersion of Mo compared to the incipient wetness impregnation method and thus, yielded higher

* Corresponding author. School of Chemical and Energy Engineering, Faculty of Engineering, Universiti Teknologi Malaysia, 81310 UTM Johor Bahru, Johor, Malaysia.
E-mail addresses: nmizzudin97@gmail.com (N.M. Izzudin), aishahaj@utm.my (A.A. Jalil).

photocatalytic activity towards simultaneous removal of TC and Cr(VI). Besides, quenching experiments revealed the electrons and holes as the active species that play a dominant role in the simultaneous photo-redox of Cr(VI) and TC. Lastly, the FSMo catalyst demonstrated high stability after four continuous cycles of simultaneous photocatalysis reactions, implying its potential as a suitable material for practical wastewater treatments.

1. Introduction

Water is a vital source that covers around 70% of the Earth's surface. However, due to the engender of water contaminants such as pharmaceutical compounds in the hydrosphere, clean water resources have been scared significantly (Seid et al., 2022). Over the years, the growth of the human population and changes in lifestyle have instigated rapid industrialization and an extensive production of pharmaceutical products around the globe (Yaashikaa and Kumar, 2022). This phenomenon has exposed the environment and humans to great danger due to the uprising of pharmaceutical compounds in the water matrix, ascribed to the uncontrollable consumption of pharmaceutical products and the discharge of partially treated pharmaceutical effluent into the water bodies (Oluwole and Olatunji, 2022). Over the years, tetracycline compound (TC) has been determined as one of the prevalent pharmaceutical compounds in the environment and has been considered one of the global threats due to its low metabolism property which makes some proportion of the consumed TC be excreted from the human body in form of feces or urine, resulting in the accumulation of TC in the aquatic domain (Zhang et al., 2021). Moreover, TC has been related to numerous health issues such as kidney and liver failure, endocrine disruptors, hepatic and some cancers which make it hazardous to humans (di Cerbo et al., 2019). Besides, a recent study reported that some heavy metal ions such as hexavalent chromium (Cr(VI)) and divalent cadmium (Cd(II)) have also been detected in the practical pharmaceutical industrial wastewater (Girish, 2020). Cr(VI) is a non-biodegradable metal ion in which its removal is an urgent matter due to its high potential for carcinogenicity, mutagenicity, toxicity, and teratogenicity properties which can give negative consequences to humans and the environment even at trace levels (Agoro et al., 2020). In addition, National Water Quality Standard (NWQS) of Malaysia has set 0.05 mg/L as a safety limit for discharging the Cr(VI) into the water bodies (Alias et al., 2020). Nevertheless, the coexistence of TC and Cr(VI) in the pharmaceutical wastewater can be a problem to the wastewater treatment process since Cr(VI) can actively react with TC to generate a complex molecule that is difficult to treat (Izzudin et al., 2021). Hence, the effective and sustainable elimination of TC and Cr(VI) from the pharmaceutical industry has become a top priority for research directions.

Numerous traditional methods have been employed over the past year to destroy the tetracycline in the aqueous system, which includes physical processes such as adsorption and membrane separation methods (Jannat Abadi et al., 2019; Zdarta et al., 2022). But, the efficiencies of these conventional wastewater treatment methods are limited by some drawbacks including the generation of secondary pollution, the complexity of the treatment process, and the time-consuming (Keerthana et al., 2022). Additionally, some of these conventional methods are inefficient for the removal of a low concentration of pollutants, which allows some residual of pollutants to be discharged into the hydrosphere, resulting in the accumulation of the pollutants in the water matrix (Azami et al., 2020). On the other hand, the removal of Cr(VI) from water also has become quite challenging nowadays. Till date, the most efficient way for dealing with Cr(VI) pollution is by reducing the high toxicity of Cr(VI) to low toxicity of Cr (III) (Yang et al., 2022).

In this context, advanced oxidation processes (AOPs) which utilized the radical species have been identified as a feasible alternative approach to the traditional wastewater remediation methods in eliminating the heavy metals and organic pollutants in the hydrosphere (Berkani et al., 2022). Furthermore, the photocatalysis reaction is one of the most widely investigated AOPs due to its environmentally friendly (Ma et al., 2020), can be operated at a mild process condition (Aziz et al., 2021b), no generation of secondary pollution (M.S. Azami et al., 2021), and remarkable potential in degrading the organic pollutants to non-hazardous materials such water and carbon dioxide (Hassan et al., 2020). Interestingly, this method is capable of effectively eliminating both organic pollutants and heavy metals. For instance, the modification of TiO_2 catalyst with activated carbon materials has shown excellent photocatalytic activity toward phenol removal (Asencios et al., 2022). Meanwhile, the fabricated g-C_3N_4/Cu-doped ZrO_2 photocatalyst also showed favorable photocatalytic activity towards Cr(VI) removal in which 90% of Cr(VI) has efficaciously been removed in this study (Reddy et al., 2022). Generally, the photocatalysis reaction is conducted for removing either heavy metal or organic pollutants at a time. Interestingly, an innovative simultaneous photocatalysis reaction has been proven to show superior photocatalytic efficiency relative to the typical photocatalysis reaction (Guo et al., 2018; Hemmati-Eslamlu et al., 2021; Jiang et al., 2021). This can be attributed to its excellent utilization of photoproduced electrons and holes, and efficient charge transferability due to the presence of the synergistic effect between oxidizable organic pollutants and reducible heavy metals.

During the last decades, numerous photocatalyst materials have been employed for photocatalysis studies. Among them, molybdenum oxide (MoO_3) is one of the intriguing materials due to its non-toxicity behavior, high photon absorption (Liu et al., 2019), anisotropic crystal growth (Cai et al., 2021), and rich oxygen vacancies (Liu et al., 2021a), and has been utilized widely as a suitable photocatalyst for the remediation of distinct organic contaminants and toxic metals. Wang and his research group have successfully developed MoO_3/Zn–Al LDHs composite photocatalyst and showed 90.5% removal of tetracycline in 60 min (Wang et al., 2021). On the other hand, Tahmasebi et al. reported the utilization of MoO_3/$Cs_3PMo_{12}O_{40}$ composite photocatalyst for rhodamine B (RhB) removal. Remarkably, this photocatalyst demonstrated 93% efficiency towards the removal of RhB under visible light irradiation (Tahmasebi et al., 2021). Meanwhile, the Z-scheme $ZnIn_2S_4$@MoO3 heterojunction photocatalyst synthesized by Ouyang et al. demonstrated 94.5% degradation of tetracycline hydrochloride (TC-HCl) in 90 min (Ouyang et al., 2021). Despite these outstanding performance of MoO_3-based photocatalysts toward removal of various water contaminants, the utilization of commercial MoO_3 in the photocatalysis study is restricted by two key drawbacks; (1) low surface area and accessibility of the active site, and (2) low quantum yield.

Recently, fibrous silica (KCC-1) has captivated a lot of attention among researchers due to its unique characteristic that promotes the generation of mesopores and micropores with bi-continuous lamellar silica fibre structures (Fauzi et al., 2022). In addition, the fibrous silica material demonstrated high surface area and abundant defect sites which is favorable for high photocatalytic activity (Hitam et al., 2020a). Previously, our group successfully synthesized several fibrous silica-metal oxide photocatalysts using a modified microemulsion method for a distinct range of water pollutants removal. For instance, Fauzi and her teammates have successfully synthesized fibrous silica-titania (FST) and showed 90% efficiency towards the degradation of ibuprofen (Fauzi et al., 2018). Besides, Rahim et al. (2020) reported 70.2% efficiency towards desulphurization of dibenzothiophene over fibrous silica tantalum (FSTa). Meanwhile, Aziz et al. (2021) reported 96% and 59% removal of Cr(VI) and p-cresol, respectively via simultaneous photocatalysis over fibrous silica zirconia (FSZr) photocatalyst (Aziz et al., 2021b). These high photocatalytic efficiencies can be

assigned to the improvement of photocatalyst properties such as lower bandgap, large surface area, low recombination of charge carriers and abundant of defects.

Despite the extensive fabrication of fibrous silica metal oxides, there is no reported study on the development of fibrous silica molybdenum oxide (FSMo) for the removal of water pollutants. Hence, inspired by these studies, we presented a novel development of nanoporous fibrous silica-molybdenum oxide (FSMo) for simultaneous TC and Cr(VI) removal. The efficiency of the FSMo catalyst towards TC and Cr(VI) abatement was compared to the MoO_3/KCC-1, KCC-1, and MoO_3 catalysts. Furthermore, the effect of parameters such as pollutant concentration, pH, and catalyst dosage on the visible-light-driven photocatalytic activities are also investigated. A possible mechanism of simultaneous photocatalysis reaction over FSMo is proposed and scrutinized in detail. It is believed that these findings will give significant information on the development of fibrous silica-based materials for wastewater remediation.

2. Experimental

2.1. Material synthesis

The commercial molybdenum oxide (MoO_3) with 99.5% purity, was obtained from Sigma Aldrich Sdn. Bhd., Malaysia. Tetraethyl orthosilicate (TEOS) and toluene with 98% and 99.5% purity, respectively were obtained from Merck Sdn. Bhd., Malaysia. Urea was acquired from Vchem Sdn. Bhd., Malaysia. Butanol (BuOH) was acquired from QRec Sdn. Bhd., Malaysia. Potassium dichromate ($K_2Cr_2O_7$) and tetracycline used as pollutant precursors were bought from Emorg Sdn. Bhd. and Chem Cruz Sdn. Bhd., Malaysia with purity 98% and 99%, respectively. Cetyltrimethylammonium bromide (CTAB) with 99% purity was bought from Fisher Scientific (M) Sdn. Bhd., Malaysia. The variation of the pH system was calibrated by adding the HCl or NaOH solution dropwise.

2.2. Synthesis of KCC-1

As previously reported by our group, fibrous silica (KKC-1) was successfully synthesized using the microemulsion approach. (Shahul Hamid et al., 2019). In a brief, about 15 g of surfactant (CTAB) together with 6 g of hydrolyzing agent (urea) were dissolved in distilled water with vigorous stirring for 1 h under room standard room conditions. After that, a 5:2 M ratio of toluene and butanol was added to the blend solution and constantly agitated for 1 h. Next, approximately 10 mL of TEOS was mixed with this mixture and agitated for 4 h prior to the heating at 423 K. Then, the solution was transferred into the beaker before let dried overnight at 383 K. After that, the white solid obtained was ground into a fine powder before undergoing heating treatment at 823 K with a ($q = 3$ K min^{-1}, $t = 8$ h).

2.3. Synthesis of composite MoO_3/KCC-1

The composite of molybdenum oxide (MoO_3) loaded onto fibrous silica (KCC-1) was synthesized by the effortless incipient wetness impregnation method (Hitam et al., 2020a). In a typical synthesis, the pristine MoO_3 was used as the Mo precursor and the preparation procedure for MoO_3/KCC-1 was as follows. Initially, MoO_3 and KCC-1 with a ratio of 0.1:1 by weight were transferred into two separate beakers containing 50 mL of distilled water and then stirred at medium speed for 30 min at 323 K. The solution containing MoO_3 catalyst was labelled as solution A. Meanwhile, the solution containing the KCC-1 catalyst was labelled as solution B. After 30 min of homogeneous stirring, solution A was then mixed with solution B and continuously stirred at 353 K for 2 h. Then, the temperature of the solution was rise to 373 K and let continuously stirred until the solution is completely dried. Next, the obtained catalyst was dried in the oven at 383 K to ensure the complete removal of residual moisture. Finally, the obtained greenish-white solid was ground

into a fine powder and calcined for 8 h (T = 823 K, q = 3 K min^{-1}).

2.4. Synthesis of FSMo

The fibrous silica-molybdenum oxide (FSMo) was prepared via in-situ microemulsion method as reported in the previous study (FSZr) (Aziz et al., 2021a). On the contrary, in this study, commercial MoO_3 was used as a seed instead of TiO_2 and the molar ratio of water to toluene was determined at 1:5. Firstly, the blend solution of mixed urea, water, and CTAB was stirred vigorously for 30 min to ensure the homogeneous mixing of the mixture. To this solution, toluene and butanol with a molar ratio of 5:2 were added and consistently stirred for 1 h. After that, the TEOS solution was added to the mixture and stirred continuously for 8 h at 423 K. Then, microwave irradiation was applied to the solution at 480 W for 2 h. A greenish-white precipitate was obtained after a centrifugation step. The greenish-white precipitate was then washed with acetone and distilled water before being dried at 383 K overnight. After that, the obtained greenish-white solid was ground into a fine powder before undergoing a calcination process under a muffle furnace at 823 K for 8 h.

2.5. Characterization of the catalysts

The phase and crystallinity of prepared catalysts were determined under X-ray diffraction (XRD) spectroscopy analysis using a diffractometer (Bruker Advance D8, USA) in the range of $2\Theta = 3°$ to $90°$. The microscopy of the surface morphology of the catalysts was evaluated using Field-emission scanning electron microscopy (JEOL JSM-6701F). The inner microstructure of the catalysts was studied using Transmission electron microscopy (JEM-ARM200F). The functional group present in the catalysts was evaluated using Fourier Transform Infrared spectroscopy (Agilent Cary 640) via KBr method in the region of 1600–400 cm^{-1}. The textural properties of catalysts were analyzed using N_2 physisorption (Thermo-Scientific Surfer). The optical and electronic properties of the catalysts were identified using ultraviolet–visible/diffuse reflectance spectra (UV–Vis/DRS, Agilent Cary 60) and Photoluminescence (PL) spectroscopy analysis (PTI Quanta-Master™ 60 Fluorescence Spectrophotometer, USA). The extrapolation of the bandgap of the prepared catalysts was determined through Kubelka-Munk (K-M) plot.

2.6. Synergistic photocatalytic remediation of Cr(VI) and TC

The photocatalytic activities of the synthesized catalysts towards simultaneous remediation of Cr(VI) and TC were investigated in a batch reactor. The metal halide lamp (400 W, $\lambda \geq 400$ nm) was utilized as the visible light source. The reactor is coupled with a cooling system to retain the room temperature condition throughout the reaction. The simultaneous photocatalytic redox experiments were preceded as follows: 0.1–0.6 g L^{-1} of catalyst was dispersed into a 100 mL mixed pollutants system of required initial concentration (Cr(VI) = 50 mL, TC = 50 mL). The pH of the pollutants (1–11) was adjusted using HCl or NaOH solutions. Prior to the visible light illumination, the solution was agitated for 1 h in the dark to achieve adsorption-desorption equilibrium. The photocatalytic experiment was conducted for 3 h at 293 K. About 2 mL of the solution was taken at the 30 min time interval and centrifuged at 750 rpm to separate the catalyst from the treated pollutant solution. The concentration of TC and Cr(VI) were analyzed using UV–Vis spectrophotometry (Cary 60 UV–Vis, Agilent Technologies, USA) at maximum wavelengths of 357 nm and 345 nm, respectively (Q. H. Li et al., 2021; Valério et al., 2020). The photocatalytic efficiency towards Cr(VI) and TC removal was evaluated using the equation below:

Photocatalytic efficiency $(\%) = (1 - C_t / C_0)$ x 100   (1)

where C_t is the pollutant's concentration at time (t) = t, and the C_0 is the initial concentration of the pollutant.

The stability of the optimum photocatalyst was evaluated for four cycles of simultaneous photo-redox of Cr(VI) and TC. At the end of every photocatalytic experiment, the photocatalyst was rinsed with HCl to eliminate the residual Cr and then let dry overnight at 383 K before being reused for the next cycle.

3. Results and discussion

3.1. Photocatalytic activity

3.1.1. Simultaneous photocatalytic redox of Cr(VI) and TC

The catalytic activity of the prepared FSMo catalyst was evaluated in visible-light illumination for the reduction of Cr(VI) and the oxidation of TC. Prior to the photocatalytic experiment, the photolysis of TC and Cr(VI) were conducted in a single pollutant system using visible light exposure to determine the self-degradability and reducibility of pollutants in the natural condition. As shown in Fig. S1, TC and Cr(VI) demonstrated 17.1% oxidation efficiency and 10.8% reduction efficiency, respectively, in the absence of photocatalyst, showing that the TC and Cr(VI) exhibited high stability in the natural water bodies. On the other hand, in the photocatalytic experiment, the adsorption-desorption equilibrium of Cr(VI) and TC was achieved after 1 h of agitation in the dark before illumination with visible light. The effectiveness of the FSMo towards the removal of TC and Cr(VI) in individual and mixed pollutants systems was evaluated as shown in Fig. 1. As clearly observed, both TC and Cr(VI) demonstrated an enhancement of photoredox efficiency in the mixed pollutants system. As noticed, the degradation efficiency of TC in single pollutant system is 46%. However, upon the addition of Cr(VI) into the system, the removal efficiency of TC was boosted at a tremendous rate (74%). Similarly, Cr(VI) showed a minimal reduction efficiency in the single pollutant system (55%). When an equivalent amount of TC solution was added to the pollutant system, the reduction efficiency of Cr(VI) increased significantly to 69%. The results obtained suggest that the synchronicity of oxidizable (TC) and reducible (Cr(VI)) species could more effectively exploit the photoinduced carrier (electrons and holes), resulting in high TC oxidation and Cr(VI) reduction performance (Zhao et al., 2019). A similar phenomenon was found when the CuBi$_2$O$_4$/calcined ZnAlBi-LDHs composite photocatalyst was utilized for simultaneous removal of TC and Cr(VI) (Zhang et al., 2022). The coexistence of TC and Cr(VI) induced the synergistic effect which resulted to high photocatalytic performance.

3.1.2. Kinetic of simultaneous photoredox of TC and Cr(VI)

The photokinetic evaluation of the FSMo was then carried out utilizing the Langmuir-Hinshelwood (L-H) model to determine its photocatalytic performance. The pseudo-first-order was calculated using Eq. (2).

$$\ln\frac{C_t}{C_0} = K_{app}t \tag{2}$$

where C_t represents the concentration at t = t, and C_o is the initial concentration of TC or Cr(VI). Meanwhile, the k_{app} is represent the pseudo-first-order reaction rate constant. The linear plot of ln (C_o/C_t) vs illumination time, as shown in Fig. 2, verifies that the simultaneous photocatalytic removal of TC and Cr(VI) over FSMo followed the pseudo-first-order kinetic model. The k_{app} calculated from the slope of the plot, as shown in Table S1, demonstrated that the FSMo has a positive and significant impact on the degradation of TC and reduction of Cr(VI). The k_{app} value decreased as the initial concentration was increased, indicating that the reaction is favorable at low concentrations. (Azami et al., 2020). Then, the L-H kinetic model was plotted based on the L-H Eq. (3) .

$$\frac{1}{k_{app}} = \frac{1}{k_r K_{LH}} = \frac{C_0}{k_r} \tag{3}$$

where k_r is the reaction rate constant (mg L^{-1} min^{-1}), K_{LH} is the TC or Cr(VI) adsorption coefficient onto the catalyst surface (L mg^{-1}), and C_0 refers to the initial concentration of TC or Cr(VI) (mg L^{-1}). The obtained values of k_r 0.5429 mg L^{-1} min^{-1} and 0.0565 mg L^{-1} min^{-1} and K_{LH} were 0.011 L mg^{-1} and 0.0002 L mg^{-1}, for TC degradation and Cr(VI) reduction, respectively. These values indicated that the TC and Cr(VI) on the catalyst surface were the reaction's controlling steps (Aziz et al., 2021a).

3.2. Characterization

3.2.1. Phase and crystallinity studies

Fig. 3a-b shows the XRD diffractogram of commercial MoO$_3$, KCC-1, MoO$_3$/KCC-1, and FSMo catalysts. The synthesized catalysts displayed a clearly defined peak at 2Θ = 10°-70°. The KCC-1 catalyst displayed a broad peak at 2Θ = 15°-30°, which represents the amorphous phase of silica structure (Shahul Hamid et al., 2019). The XRD analysis confirmed the orthorhombic structure of α-MoO$_3$ and this result matched well with the JCPDS data (Card no. 050508) (Prakash et al., 2019). Several crystallite peaks appeared at 2Θ = 12.9°, 23.4°, 25.8°, 27.4, 33.7°, 39.0°, 46.1° and 49.4° in MoO$_3$/KCC-1 and FSMo catalysts are corresponded to the crystal plane of (020), (110), (040), (021), (111), (041), (200) and (002). The FSMo catalyst displayed a much lower intensity of crystallite peaks than the MoO$_3$/KCC-1 catalyst, signifying that the in-situ synthesis method (FSMo) promoteds well-dispersion of Mo element on the silica framework compare to the incipient wetness impregnation method (MoO$_3$/KCC-1) (Bahari et al., 2022; Hitam et al., 2020b).

3.2.2. FTIR spectroscopy analysis

The analysis of Fourier Transform Infrared (FTIR) spectroscopy was conducted to explore the functional group that exists in the prepared catalysts. Fig. 4A displayed the FTIR spectra of the prepared catalysts in the range of 400–1600 cm^{-1}. The KCC-1 shows four distinct bands at 460, 797, 964, and 1084 cm^{-1}, which revealed the presents of Si–O–Si bending, Si–O–Si symmetric, Si–OH, and Si–O–Si asymmetric, respectively (M. S. Azami et al., 2021; Hitam et al., 2020b). Meanwhile, the pristine MoO$_3$ displays 4 major bands at 484, 588, 865, 994, and 1106 cm^{-1}. The broad peak at 484 and 588 cm^{-1} are assigned to the bending and stretching vibration of the O–Mo–O functional group (Hu et al., 2015). The stretching mode of Mo=O oxygen terminal at peak 994 cm^{-1} revealed the orthorhombic layered of the MoO$_3$ phase (Hojabri et al., 2015). The Mo–O–Mo stretching mode was represented by the peak at 865 cm^{-1}. A notable decrease in peaks intensity is observed for Si–O–Si bending Si–OH, Si–O–Si, and Si–O–Si symmetric group of MoO$_3$/KCC-1 and FSMo catalysts, which can be assigned to the interaction between the fibrous silica framework and Mo element upon been introduced by both in-situ microemulsion and incipient wetness impregnation methods (Fatah et al., 2020).

For further study on the chemical composition of the catalysts, the bands at 1400–1000 cm^{-1}, 1000-900 cm^{-1}, and 600–400 cm^{-1} were deconvoluted by the Gaussian curve fitting (Fig. S2) and the results were interpreted and presented in Fig. 4B-D. The deconvoluted of 1084 cm^{-1} demonstrated five major bands at 1233, 1163, 1106, 1074, and 1045 cm^{-1}, which correspond to the Si–O–Si longitudinal optical asymmetric, fewer cross-linked stretching, linear structure stretching, and transversal optical asymmetric, respectively (Hitam et al., 2020b). The intensity of these bands reduced significantly upon the introduction of Mo species, signifying that which can be assigned to the formation of Si–O–Mo interaction. It was also observed that the Si–O–H and Si–O bands at 968 cm^{-1} and 945 cm^{-1} declined at once after the addition of the Mo element. An emergence of the band at 945 cm^{-1} was also observed, which attributed to the formation of Si–O–Mo bond. On the other hand,

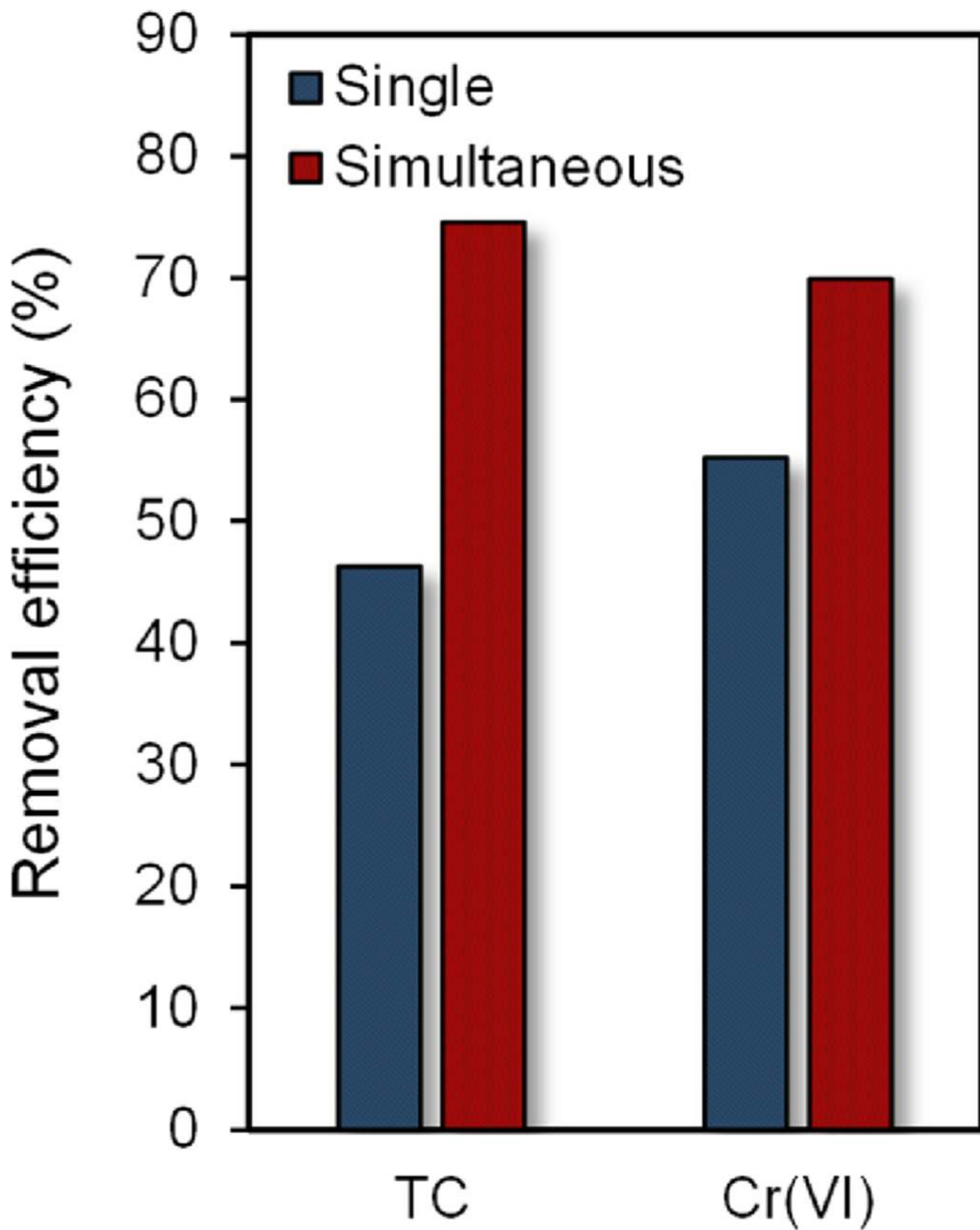**Fig. 1.** Photocatalytic removal efficiency of TC and Cr(VI) in single and simultaneous system under visible light irradiation (W = 0.375 g L^{-1}, TC = 10 mg L^{-1}, Cr (VI) = 10 mg L^{-1}, pH = 9, t = 3 h).
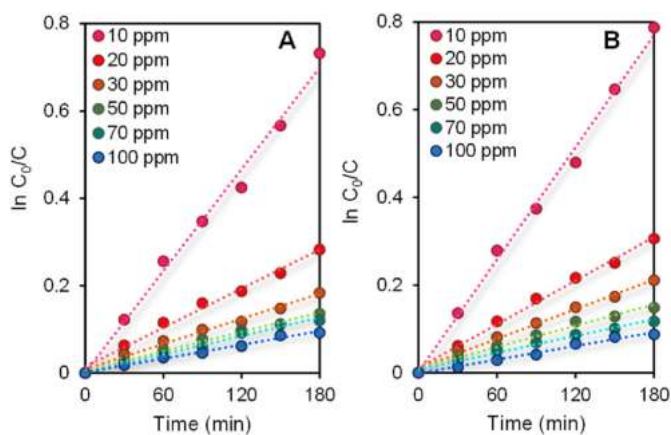
Fig. 2. Kinetic photo-redox of (A) TC and (B) Cr(VI) at different initial concentration in the simultaneous system over FSMo catalyst (W = 0.375 g L^{-1}, pH = 9, t = 3 h).
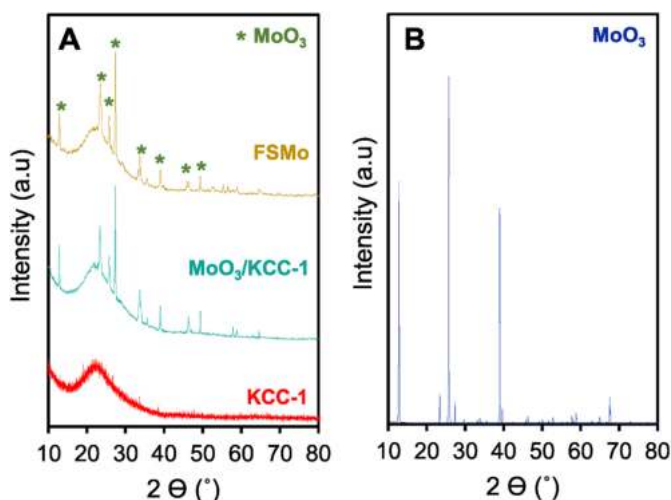

Fig. 3. XRD diffractogram of prepared catalysts.

Fig. 4. (A) The FTIR spectra of (a) KCC-1, (b) MoO$_3$, (c) MoO$_3$/KCC-1, and (d) FSMo catalyst; Gaussian peak area of FTIR deconvolution peak and intensity of the bands at (B) 1400–100 cm^{-1}, (C) 1000-900 cm^{-1}, and (D) 600–400 cm^{-1}.

MoO$_3$/KCC-1 demonstrated a much lower intensity of Si–O–Si at band 467 cm^{-1} compared to the FSMo, which might be due to the distortion of the fibrous silica framework when introducing the Mo element via the incipient wetness impregnation method (Hassan et al., 2022; Shahul Hamid et al., 2019).

3.2.3. Morphological studies

The surface morphology of the prepared catalysts (MoO$_3$, KCC-1, MoO$_3$/KCC-1, and FSMo) have been studied by FESEM and TEM analyses. As shown in Fig. 5A, the pristine MoO$_3$ catalyst exhibited irregular and stacked flake-like morphology with a relatively smooth surface (Li et al., 2017). On the other hand, the synthesized KCC-1 presented in Fig. 5B demonstrated a spherical morphology of well-ordered dendrimeric silica fiber with particle sizes ranging from 400 to 600 nm, which is similar to those reported in the previous studies (Aziz et al., 2018; Fauzi et al., 2018). Meanwhile, upon the addition of the Mo element (Fig. 5C) onto the cockscomb-like silica surface via the incipient wetness impregnation method, the spherical morphology of fibrous silica is still retained but slightly distorted which can possibly be assigned to the interaction between Mo element and the surface of Si–O–Si framework (Hitam et al., 2020b). This finding is similar to the previously reported study on the development of metal oxide loaded/KCC-1 for carbon dioxide methanation, in which the fibrous morphology remains intact with a slight change in its sphericity upon the addition of metal element
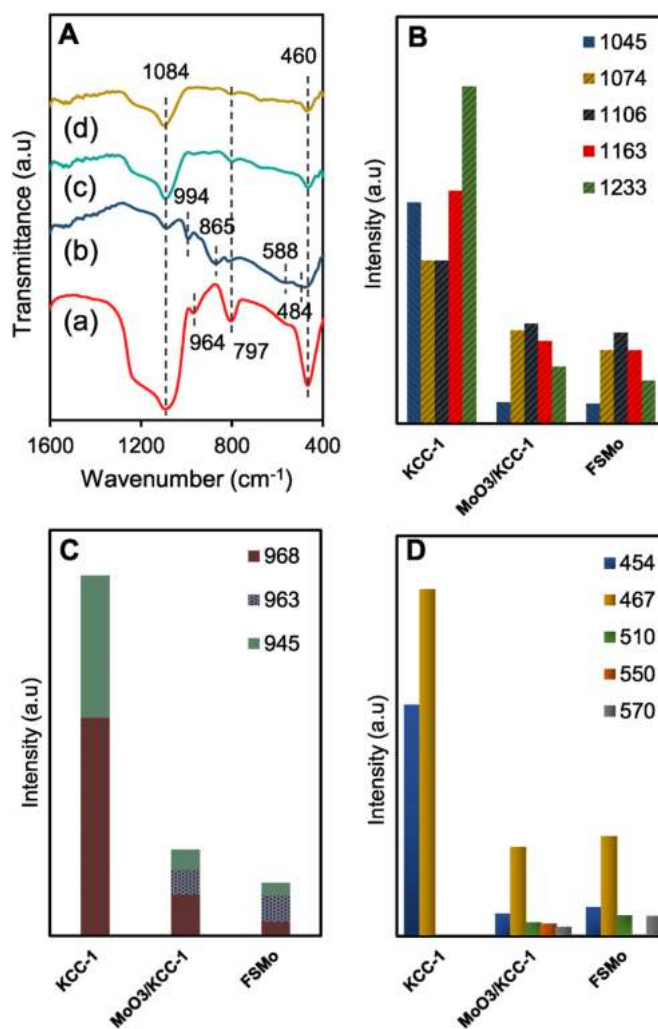
on the KCC-1 by the incipient wetness impregnation method (Shahul Hamid et al., 2018). For the FSMo catalyst (Fig. 5E), it is observed that the morphology of this catalyst is identical to the KCC-1 catalyst, confirming a well-preserved fibrous structure upon the addition of MoO$_3$ seed via the in-situ method. Moreover, FSMo demonstrated highly dispersion of Mo element (Fig. 5F) compared to the MoO$_3$/KCC-1 (Fig. 5D), describing that the FSMo shows the spatial distribution and close contact of MoO$_3$ with dendrimeric silica fiber during the in-situ microemulsion method, which is in accordance with the result in XRD analysis.

Further study on the morphology of FSMo catalyst has been carried out by TEM analysis. Similar to the previous study, the TEM image of prepared FSMo (Fig. 6A), demonstrated a high-resolution image of preserved fibrous silica framework, which indicated the successful development of fibrous silica-molybdenum oxide photocatalyst (Fauzi et al., 2020b). Furthermore, the elemental mapping on the FSMo catalyst revealed the uniformly disperse of Si, O, and Mo elements in the FSMo catalyst, suggesting that the synthesis of silica-molybdenum oxide catalyst via the microemulsion method resulted in well-dispersion of Mo element onto the fibrous structure (M.S. Azami et al., 2021). The well-dispersion of Mo in the FSMo may play a vital role in achieving high photocatalytic activity towards simultaneous photo-redox of Cr(VI) and TC. Meanwhile, the EDX analysis (Fig. 6E) unveiled the intensity of Si, O, and Mo elements in the FSMo catalyst. As clearly shown, the Si elements
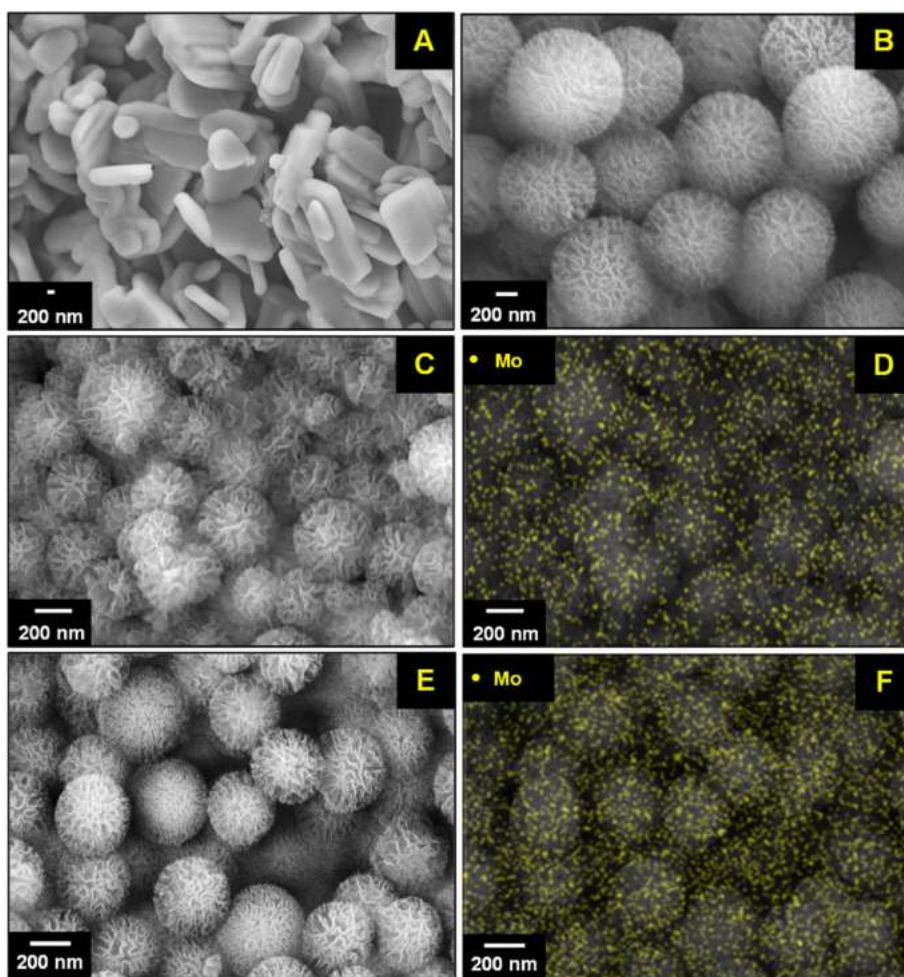
Fig. 5. FESEM images of (A) MoO_3, (B) KCC-1, (C–D) MoO_3/KCC-1 with elemental mapping Mo, and (E–F) FSMo with elemental mapping Mo.
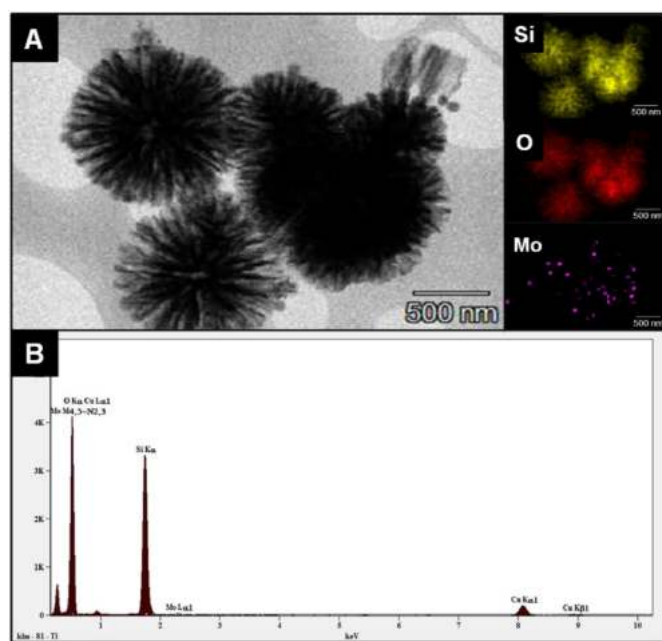

Fig. 6. (A) The TEM image of FSMo with elemental distribution of (B) O, (C) Si and (D) Mo; and (E) EDX analysis of FSMo catalyst.

demonstrated the highest intensity elements in the FSMo, attributed to the large fibrous silica framework. On the other hand, high intensity of O element was observed in the FSMo catalyst compared to the Mo element which can be reasoned to the presence of excess oxygen during the calcination process which resulted in the high concentration of surface oxygen (Fu et al., 2022).

3.2.4. Textural studies

The textural properties of synthesized catalysts were studied by N_2 adsorption-desorption isotherm analysis as shown in Fig. 7. According to the IUPAC, the isotherms of all catalysts can be classified as type IV, indicating that these catalysts exhibited mesoporous structures (Baca et al., 2020; Yan et al., 2020). In addition, the specific surface area and interparticle pores for the MoO_3 were substantially increased after the introduction of the fibrous silica framework, suggesting that the fibrous silica provides a high surface area and accessible active sites for more contact between the targeted pollutants and photocatalyst (M. S. Azami et al., 2021). Nevertheless, the FSMo catalyst demonstrated a much lower surface area and total pore volume compared to the MoO_3/KCC-1 catalyst which can possibly be due to the presence of the Mo element in the fibrous silica framework. This is in agreement with the morphological results from FESEM and XRD analysis. The N_2 adsorption-desorption analysis showed an average pore diameter <50 nm for all catalysts, revealing the nanoporous structure of the synthesized catalysts. Table 1 summarized the textural properties as well as the bandgap of all the catalysts.
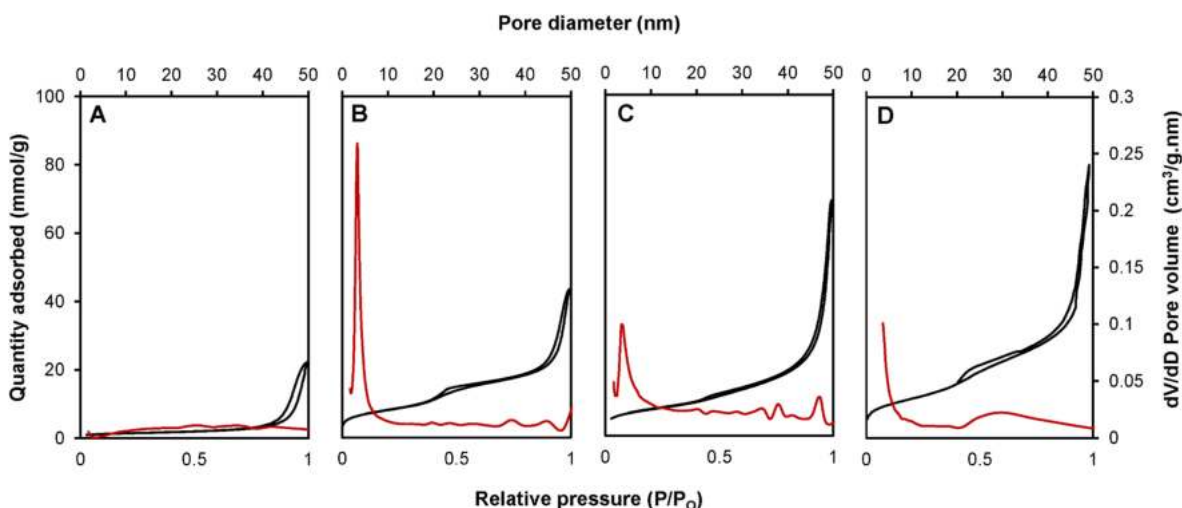
Fig. 7. BJH pore size distribution and N_2 adsorption-desorption isotherms of (A) KCC-1 (B) MoO_3 (C) MoO_3/KCC-1 and (D) FSMo.

Table 1
The textural and optical properties of all catalysts.

Photocatalyst	Surface area[a] (m^2/g)	Total pore volume (cm^3/g)	Avg. pore diameter (nm)	Bandgap[b] (eV)
MoO_3	114	0.77	27.1	2.21
KCC-1	632	1.71	9.55	3.75
MoO_3/KCC-1	610	2.39	15.7	1.90
FSMo	417	1.14	17.9	2.12

[a] Calculated from N_2 adsorption measurements using the BET method.
[b] Calculated using Kubelka-Munk Equation.

3.2.5. Optical and photoluminescence spectroscopy studies

The optical property and charge separation efficiency of the catalysts were evaluated via Photoluminescence (PL) spectroscopy and Ultraviolet–Visible Diffuse Reflectance Spectra (UV–Vis/DRS) analyses, respectively. The UV–Vis/DRS analysis was conducted to determine the bandgap of all catalysts by using the Kubelka-Munk equation as follows:

$$(ahv)^2 = A(hv - E_g) \tag{4}$$

where E_g = bandgap energy, ν = light frequency, A = absorbance (cm^{-1}), and h = Planck constant. As shown in Fig. 8A, the KCC-1 catalyst demonstrated exceptional large bandgap energy (3.75 eV), depicting its
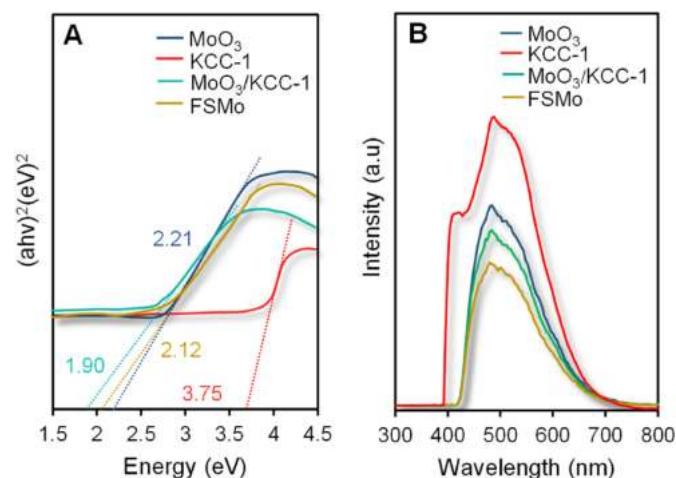

Fig. 8. (A) Plot of transformed Kubelka-Munk function versus the energy of light; and (B) Photoluminescence spectra of all catalysts.

inadequacy as photocatalyst material for the visible light region. Meanwhile, the MoO_3 demonstrated as a highly-photosensitivity material with relatively low bandgap energy (2.21 eV). This finding matched well with the reported study by Mafa in 2021 (2.40 eV) (Mafa et al., 2021). In addition, red-shifts in the absorption edge were observed for FSMo and MoO_3/KCC-1 catalysts, possibly due to the formation of defects during the synthesis of composite catalysts which narrowed the bandgap energy level (Liu et al., 2021b). The FSMo and MoO_3/KCC-1 catalysts demonstrated 2.12 eV and 1.90 eV of bandgap energy, respectively.

Besides, photoluminescence (PL) analysis is an archetypal technique used in the photocatalysis study to observe the recombination rate of photogenerated charges, revealing the effectiveness of migration, and separation of charge carriers transfer in the photocatalyst. The catalysts were excited with the laser line at 350 nm at the emission region of 300–800 nm as presented in Fig. 8B (Joya et al., 2019). The catalysts showed emission The KCC-1 catalyst demonstrated the highest intensity of peak at 487 nm, signifying the high recombination rate of photoproduced charges. This can be assigned to the large bandgap of the KCC-1 catalyst, which provides a significant hindrance and required more energy for the excitation of the electron to the conduction band of the catalyst. Thus, the excited electrons in the KCC-1 catalyst tend to recombine back with the photogenerated holes. Likewise, the PL spectrum of pristine MoO_3 showed a much lower intensity peak relative to the KCC-1 catalyst which might be correlated to the high crystallinity of the MoO_3 catalyst which provided well dispersion of the excited electron on the conduction band (Liu et al., 2021b). On the other hand, a substantial improvement in the solar utilization efficiency and charge separation rate was observed upon the introduction of MoO_3 to the silica framework which can be assigned to the migration of charges in the composite catalysts, resulting in efficient charge separation and high photocatalytic efficiency (Xiao et al., 2022). However, the composite MoO_3/KCC-1 catalyst demonstrated a slightly higher intensity of PL than the FSMo catalyst which might be due to the poor dispersion of Mo element on the KCC-1 catalyst, which acted as a new recombination center for electrons and holes, resulting in low charges separation efficiency (Adhikari et al., 2020). The FSMo exhibited the lowest PL intensity, demonstrating it as a potential photocatalyst material with excellent charge separation. Similar cases also have been reported by Fauzi et al. (2020) and Azami et al. (2022) where the fibrous silica metal oxides showed much lower PL intensity compared to the commercial ones which can be attributed to the suppression of recombination between photoexcited electron and hole pairs (M.S. Azami et al., 2022; Fauzi et al., 2020a).

3.3. Effect of parameters towards simultaneous photoredox TC and Cr (VI)

3.3.1. Effect of pH

In general, TC exists in four different structures in a different range of pH, in which each structure possesses a different charge state. Interestingly, TC exists predominantly as a monovalent cation (pH < 3.0), a zwitterion (pH = 3.3–7.7), a monovalent anion (pH = 7.7–9.7) and a bivalent anion (pH > 9.7) (Bembibre et al., 2022). Based on the complication property of TC at different pH, therefore, it can be deduced that the pH of the pollutant system greatly affects the photocatalytic performance.

The effect of pH on simultaneous photocatalytic removal of TC and Cr(VI) using FSMo catalyst was inspected by adjusting the pH value from 3 to 11 at an initial concentration of 10 mg L^{-1} for both pollutants and 0.375 g L^{-1} dosage of catalyst as depicted in Fig. S1. Obviously, the FSMo catalyst demonstrated high photocatalytic activity towards TC degradation in medium alkaline conditions. The degradation efficiency of TC increased as the pH of the system increased up to pH 9. However, beyond pH 9, a tremendous decline in the photocatalytic efficiency toward TC removal was observed. This result can be attributed to the characteristic of the negative charges of TC at pH > 9, which reduced the adsorption of TC onto the catalyst surface, resulting in low photocatalytic activity.

Meanwhile, the reduction of Cr(VI) to Cr(III) is typically favored in the acidic condition (pH < 3) due to the abundant presence of H$^+$ can facilitate the reduction of Cr(VI) oxyanions. The mechanism of reduction Cr(VI) in the acidic condition proceeds as follows:

$$H_2CrO_4 + 6H^+ + 3e^- = Cr^{3+} + 4H_2O \tag{5}$$

or

$$HCrO_4^- + 7H^+ + 3e^- = Cr^{3+} + 4H_2O \tag{6}$$
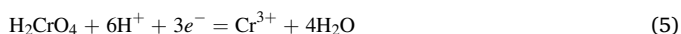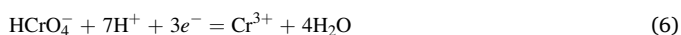
In the alkaline condition, the presence of excessive OH$^-$ ions would suppress the reduction of Cr(VI) as follow:

$$CrO_4^{2-} + 4H_2O + 3e^- = Cr(OH)_3 + 5OH^- \tag{7}$$
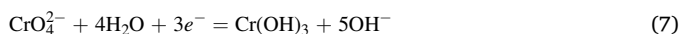
The photoreduction of Cr(VI), however, showed increasing efficiency with the increased pH up to pH 7. This could be owing to a synergistic interaction between TC and Cr(VI), which allows the photoinduced charges to be separated efficiently. Consequently, increase the number of free electrons which results in better photoreduction efficiency towards Cr(VI) removal. Similarly, at alkaline pH (pH > 7), the high concentration of OH$^-$ in the aqueous system demonstrated a significant hindrance to the intimate contact between Cr(VI) ions and the catalyst surface which in turn, slowed down the reduction activity of Cr(VI).

3.3.2. Effect of catalyst dosage

The effect of catalyst dosage on simultaneous photocatalytic removal of TC and Cr(VI) was investigated in this study in which the photocatalysis reaction was carried out under different amounts of catalyst dosage. As illustrated in Fig. S2, the FSMo catalyst demonstrated an increasing trend for TC and Cr(VI) removal when the catalyst dosage increased up to 0.375 g L^{-1}. A noticeable decline in the removal efficiency for both TC and Cr(VI) was observed when the dosage of catalyst exceed 0.375 g L^{-1} was used, suggesting that the excessive dosage of catalyst increase the turbidity of the solution and hindered the penetration of light to the catalyst surface, resulting to low photocatalytic activity (Heidarpour et al., 2020). However, the 0.625 g L^{-1} catalyst dosage demonstrated much higher total efficiency towards simultaneous removal of TC and Cr(VI) which was mainly contributed by the high adsorption of pollutants to the catalyst surface. Yet, its efficiency on the photocatalysis reaction basis is still lower than that of 0.375 g L^{-1} due to the blockage of active sites by adsorbed pollutants (Song et al., 2022). This finding evinces that 0.375 g L^{-1} is the optimum dosage for this simultaneous photocatalytic reaction.

3.4. Photocatalytic efficiency of all prepared catalyst

To prove the effectiveness of the FSMo catalyst towards simultaneous remediation of TC and Cr(VI), the simultaneous photocatalysis reaction over commercial MoO$_3$, KCC-1, and MoO$_3$/KCC-1 catalysts were also performed (Fig. S3). The KCC-1 catalyst demonstrated the lowest photocatalytic activity towards simultaneous removal of TC (46%) and Cr (VI) (24%), possibly due to the poor visible light utilization and rapid recombination rate of the photoinduced charges (Fig. 6A and B). In contrast, FSMo and MoO$_3$/KCC-1 catalysts exhibit high photocatalytic activity towards the removal of Cr(VI) and TC, been FSMo yields the highest efficiency towards oxidation of TC (75%) and reduction of Cr (VI) (69%). This result can be attributed to the narrow bandgap energy and efficient separation of photogenerated electron-hole pairs. Likewise, MoO$_3$/KCC-1 showed much lower photocatalytic activity relative to the FSMo catalyst which can possibly be attributed to the low dispersion of Mo element onto fibrous silica framework, which introduced a new recombination center, in turn, facilitates the recombination of photogenerated charges, resulting in low photocatalytic activity (Zhou et al., 2022).

The simultaneous photocatalytic removal of TC and Cr(VI) was compared with various previous photocatalysts to prove the efficacy of the FSMo catalyst, as depicted in Table 2. Based on the results, it can be said that the efficiency of simultaneous photocatalytic removal of TC and Cr(VI) over FSMo was comparable with other photocatalyst materials.

3.5. Photocatalytic mechanism

To expose the mechanism of simultaneous photo-redox of Cr(VI) and TC over FSMo, the dominant species that actively participate in the photocatalysis process were explored through quenching experiments. In this study, methanol (Met), potassium carbonate (PC), and potassium iodide (PI) were used as quenchers for the photogenerated hole (h$^+$), photogenerated electron (e$^-$), and hydroxyl radical on the surface (•OH$_{ads}$), respectively (M. S. Azami et al., 2022; Hassan et al., 2021). As depicted in Fig. 9, a notable decline in the degradation efficiency of TC was observed when Met and PI were added to the pollutants system. This result concluded that the TC undergoes oxidation process at the valence band of FSMo and photogenerated h$^+$ and •OH$_{ads}$ are the active species in the TC degradation. On the other hand, the removal percentage of Cr (VI) declined from 69% to 14% when PC was added to the pollutants system, inferring that the photogenerated e$^-$ is the dominant species for the photoreduction of Cr(VI). Meanwhile, the reduction efficiency of Cr (VI) decrease insignificantly along with the oxidation of TC when PI was added, suggesting that the •OH$_{ads}$ do not actively participate in the photoreduction of Cr(VI). The high utilization of e$^-$ at the conduction band (CB) for the reduction of Cr(VI) reduced the recombination of photoinduced charges which resulted in more free h$^+$ species. However, when the e$^-$ quencher was added to the system, the oxidation of TC is not significantly affected suggesting that the e$^-$ is not actively participated in the oxidation of TC. Based on the result obtained, it is concluded that h$^+$ and •OH$_{ads}$ played a major role in TC photo-oxidation, while e$^-$ dominated Cr(VI) photo-reduction.

For better comprehension of the simultaneous photo-redox mechanism of TC and Cr(VI) over FSMo, the valence band (VB) and conduction band (CB) positions should be calculated. The location of CB and VB of FSMo were calculated by using the Mulliken electronegativity concept as shown in the following equation (Wei et al., 2019):

$$E_{CB} = X - E_C - 0.5E_g \tag{8}$$

$$E_{VB} = E_{CB} + E_g \tag{9}$$

Table 2

Comparison of simultaneous photocatalytic removal TC and Cr(VI) over various photocatalysts.

Photocatalyst	Initial concentration (mg L^{-1})	Dosage (g L^{-1})	pH	Light source	Removal efficiency (%)	Reference
FSMo	Cr(VI): 10	0.38	9.0	Visible light	69.5	This work
	TC: 10				75.0	
MIL-125-NH$_2$@BiOI	Cr(VI): 80	1.00	NA	Visible light	80.0	Dai et al. (2022)
	TC: 80				81.0	
CQDs/HBWO-18	Cr(VI): 5	1.00	5.4	Visible light	84.5	(C. Li et al., 2021)
	TCH: 20				83.0	
rGO@ZnAlTi-LDO	Cr(VI): 5	0.40	7.0	Visible light	52.5	Ye et al. (2019)
	TC:10				80.0	
AgI/BiVO$_4$	Cr(VI): 15	0.40	NA	Visible light	70.0	Zhao et al., 2019
	TC: 20				88.0	
ZnO/rGO	Cr(VI): 20	0.05	NA	Visible light	84.0	Kumar et al. (2020)
	TC: 20				68.0	
Bi$_2$MoO$_6$@DE	Cr(VI): 60	1.00	NA	Visible light	90.1	Wan et al. (2020)
	TC: 50				74.7	
AIS/BWO	Cr(VI): 10	0.30	NA	Visible light	64.0	Zhang et al. (2019)
	TCH: 10				92.0	

*NA: not state in the literature, *Cr(VI):* hexavalent chromium, *TC:* tetracycline, *TCH:* tetracycline hydrochloride.
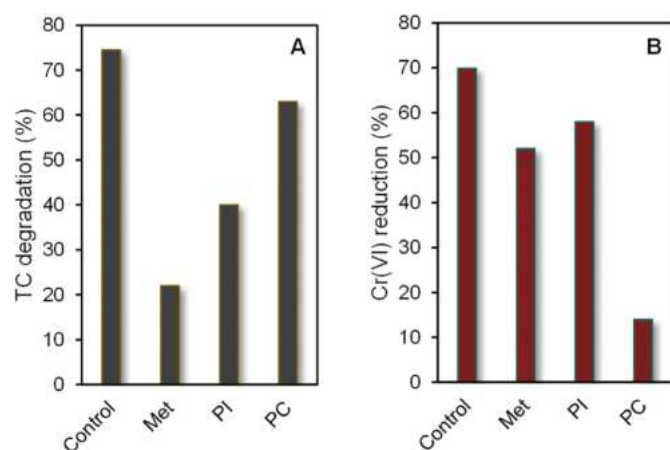

Fig. 9. Scavenger effect on simultaneous photoredox of (a) TC and (b) Cr(VI) over FSMo catalyst (TC = 10 mg L^{-1}, Cr(VI) = 10 mg L^{-1}, W = 0.375 g L^{-1} pH = 9, t = 3 h).

where E_{CB} and E_{VB} are the conduction and valence band potentials, respectively; E_g is the bandgap energy of the semiconductor; X is the absolute electronegativity of the elements, while E_C is the energy of free electron on the hydrogen scale (4.5 eV).
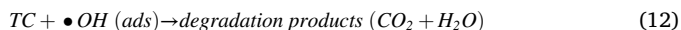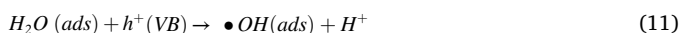
By using Eqs. (8) and (9) and the bandgap energy of FSMo from Table 1 (2.12 eV). Hence, the calculated CB and VB potentials of FSMo were 0.81 eV and 2.93 eV, respectively.

On the basis of these results, a mechanism for the simultaneous photocatalytic remediation of TC and Cr(VI) over FSMo was proposed and briefly described in Scheme 1. Briefly, the cationic TC was drawn towards highly anionic Cr(VI) which then attracted to the positively charged surface of FSMo under the dark conditions. Under the visible light illumination, the FSMo catalyst absorbed the light irradiation and spontaneously excited to the CB. Synchronously, an equivalent amount of photogenerated h$^+$ is formed at the VB. According to the calculated band energies, $\bullet$O$_2^-$ as well as the $\bullet$OH$_{bulk}$ were not produced in this photocatalysis reaction due to the E_{CB} value of FSMo was higher compared to the standard redox potential of O$_2$/$\bullet$O$_2^-$ ($E^\theta = -0.046$ eV vs. NHE) (Jiang et al., 2021). Likewise, the oxidation potential of H$_2$O/$\bullet$OH ($E^\theta = +2.40$ eV vs. NHE) is more negative than the VB potential of FSMo (Jiang et al., 2021). Hence, the photogenerated h$^+$ can
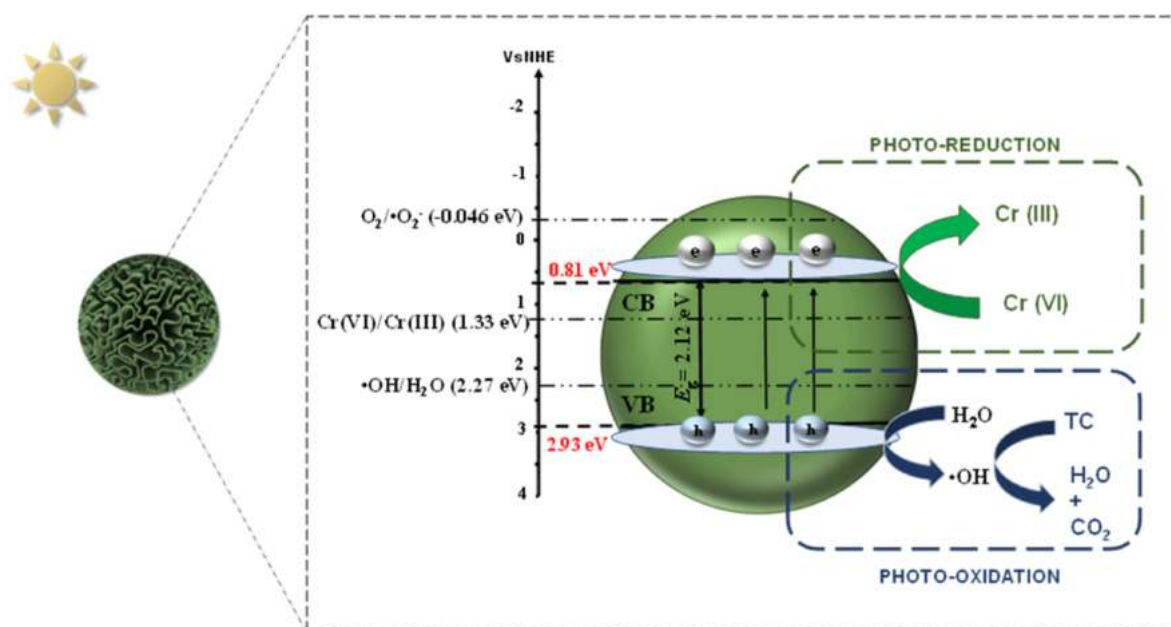
Scheme 1. Proposed mechanism of FSMo over simultaneous photo-redox of TC and Cr(VI).

oxidize the water molecules (H_2O) to hydroxyl radical (•OH) species, which isfurther utilized for the degradation of TC molecules. The mechanisms involved in the TC degradation are showed in the Eqs. 10 and 11 below.

$$FSMo + hv \rightarrow e^-(CB) + h^+(VB) \tag{10}$$

$$H_2O\ (ads) + h^+(VB) \rightarrow \ \bullet OH(ads) + H^+ \tag{11}$$

$$TC + \bullet OH\ (ads) \rightarrow degradation\ products\ (CO_2 + H_2O) \tag{12}$$

Meanwhile, since the $\bullet O_2^-$ was not produced in this reaction, hence more excited e^- are utilized for the reduction of Cr(VI) due to the CB level of FSMo is more negative than the reduction potential of Cr(VI)/Cr (III) ($E^\Theta = +1.33$ eV vs. NHE) (Aziz et al., 2021a). In addition, owing to the high utilization of e^- for reduction of Cr(VI), the recombination rate of photogenerated h^+ and e^- is reduced, resulting in high photocatalytic activity of FSMo towards simultaneous removal of TC and Cr(VI). Similarly, The mechanisms for Cr(VI) reduction to Cr(III) are shown in Eqs. 13–16 (Kumar et al., 2020). As the light penetrated the FSMo surface, the electron-hole pairs (excitons) is formed, in which the excited e^- is dispersed to the CB of FSMo. At the same time, some of the excited e^- are used to reduce the Cr(VI) to Cr(V). Then, the mechanisms of chromium reduction are continued until the Cr(VI) was successfully reduced to Cr(III). Since the e^- at CB are not been utilized for any reaction, the e^- was then recombined with the photoproduced h^+at the VB.

$$Cr(VI) + e^-(CB) \rightarrow Cr(V) \tag{13}$$

$$Cr(V) + e^-(CB) \rightarrow Cr(IV) \tag{14}$$

$$Cr(IV) + e^-(CB) \rightarrow Cr(III) \tag{15}$$

$$2H_2O + 4h^+(VB) \rightarrow O_2 + 4H^+ \tag{16}$$

3.6. Stability and reusability of the catalyst

Photocatalyst reusability is a crucial criterion for commercial-scale uses of such materials, as well as their significant economic worth (Liu et al., 2020). The reusability of the synthesized FSMo photocatalyst was evaluated for four continuous cycles (Fig. S4). The prepared FSMo catalyst demonstrated high stability towards simultaneous remediation of Cr(VI) and TC. A minor reduction in the removal efficiency was clearly observed for Cr(VI) reduction and TC degradation after four cycles of photocatalytic experiments. The obtained reduction percentages for Cr(VI) photocatalytic reduction are 69% (1st cycle), 66% (2nd cycle), 63% (3rd cycle), and 56% (4th cycle). The obtained degradation percentages of TC at the different runs are 74% (1st cycle), 70% (2nd cycle), 67% (3rd cycle), and 59% (4th cycle). The reduction in the removal efficiency could be attributed to the aggregation of the catalyst, which led to the reduction of surface area and accessibility of the active sites (M.S. Azami et al., 2022). Moreover, the FTIR pattern (Fig. S6A) and FESEM image (Fig. S6B) of the spent FSMo, showed no emergence of new peak and preservation of the spherical fibrous structure, respectively, suggesting that the approximately chemical stable and high durability of FSMo was stable for simultaneous photoredox of Cr(VI) and TC. In addition, the intensity of FTIR for spent FSMo reduced substantially compared to the fresh FSMo which is possibly due to a slight distortion of silica matrix. These findings have proved the potential of FSMo photocatalyst as a suitable candidate for practical wastewater remediation.

3.7. Practicability of the FSMo

The real pharmaceutical wastewater consists of a very complex matrix of organic compounds, dissolved organic matter and inorganic ions, heavy metal ions, etc. Some of these components might affect the photocatalytic efficiency towards the removal of water pollutants. Hence, to evaluate the real practical applicability of the FSMo catalyst, the photocatalytic experiment of multi-pollutants was carried out by adding the Ibuprofen (IBU) to the Cr(VI)-TC pollutants system. The result presented in Fig. S7 showed that the removal efficiency of Cr(VI), TC and IBU in the multi-pollutants system over FSMo catalyst is 55.2%, 63.2% and 50.2%, respectively. The decrement of photocatalytic efficiency for removal of Cr(VI) and TC in the multi-pollutants system could be ascribed to the limited reactive oxygen species (ROS) produced during the photocatalysis reaction which induced the competition between the pollutants for the reactive species. Hence, leading to low photoredox efficiency.

4. Conclusion

In conclusion, the FSMo catalyst was successfully synthesized via the microemulsion technique. The FESEM morphology demonstrated FSMo catalyst with molybdenum oxide as its core and encapsulated by the fibrous silica framework with particle sizes ranging from 500 to 600 nm. The N_2 adsorption-desorption analysis further confirmed the nanoporous structure of the FSMo catalyst with an average pore diameter of 15.7 nm. The prepared FSMo catalyst exhibits a narrow bandgap (2.12 eV) and high surface area (417 m^2/g), which signifies the successful fabrication of fibrous silica-molybdenum oxide framework. Furthermore, under visible light irradiation, the FSMo catalyst showed remarkable performance in simultaneous photocatalytic oxidation of TC (75%) and reduction of Cr(VI) (69%) compare to the pristine MoO_3, KCC-1, and MoO_3/KCC-1 catalysts which can be ascribed to its unique structure, which includes increased crystallinity, a bigger total pore volume, and a well-dispersed of Mo element. The quenching experiment revealed that the photogenerated electron was the most important species in Cr(VI) photoreduction, whereas h^+ and $\bullet OH_{ads}$ radicals were important species in TC photooxidation. Finally, it could be summarized that the modification of the MoO_3 structure encapsulated by the fibrous silica framework, would provide critical information in designing a potential photocatalyst for wastewater remediation.

Declaration of competing interest

The authors declare that they have no known competing financial interests or personal relationships that could have appeared to influence the work reported in this paper.

Data availability

No data was used for the research described in the article.

Appendix A. Supplementary data

Supplementary data to this article can be found online at https://doi.org/10.1016/j.chemosphere.2022.136456.

References

Adhikari, S., Lee, H.H., Kim, D.H., 2020. Efficient visible-light induced electron-transfer in Z-scheme $MoO_3/Ag/C_3N_4$ for excellent photocatalytic removal of antibiotics of both ofloxacin and tetracycline. Chem. Eng. J. 391 https://doi.org/10.1016/j.cej.2019.123504.

Agoro, M.A., Adeniji, A.O., Adefisoye, M.A., Okoh, O.O., 2020. Heavy metals in wastewater and sewage sludge from selected municipal treatment plants in eastern cape province, South Africa. Water (Switzerland) 12. https://doi.org/10.3390/w12102746.

Alias, N., Rosli, S.A., Abu, N., Sazalli, H., Hamid, H.A., Arivalakan, S., Nur, S., Umar, H., Khim, B.K., Taib, B.N., Keat, Y.K., Razak, K.A., Yee, Y.F., Hussain, Z., Bakar, A., Kamaruddin, N.F., Manaf, A.A., 2020. 15. Metal Oxide for Heavy Metal Detection and Removal, Metal Oxide Powder Technologies. INC. https://doi.org/10.1016/B978-0-12-817505-7.00015-4.

Asencios, Y.J.O., Lourenço, V.S., Carvalho, W.A., 2022. Removal of phenol in seawater by heterogeneous photocatalysis using activated carbon materials modified with TiO2. Catal. Today 388–389, 247–258. https://doi.org/10.1016/j.cattod.2020.06.064.

Azami, M.S., Jalil, A.A., Hitam, C.N.C., Hassan, N.S., Mamat, C.R., Adnan, R.H., Chanlek, N., 2020. Tuning of the electronic band structure of fibrous silica titania with g-C_3N_4 for efficient Z-scheme photocatalytic activity. Appl. Surf. Sci. 512, 145744 https://doi.org/10.1016/j.apsusc.2020.145744.

Azami, M.S., Jalil, A.A., Hassan, N.S., Hussain, I., Fauzi, A.A., Aziz, M.A.A., 2021. Green carbonaceous material–fibrous silica-titania composite photocatalysts for enhanced degradation of toxic 2-chlorophenol. J. Hazard Mater. 414, 125524 https://doi.org/10.1016/j.jhazmat.2021.125524.

Azami, M.S., Jalil, A.A., Aziz, F.F.A., Hassan, N.S., Mamat, C.R., Fauzi, A.A., Izzudin, N.M., 2022. Exploiting the potential of silver oxo-salts with graphitic carbon nitride/fibrous silica-titania in designing a new dual Z-scheme photocatalyst for photodegradation of 2-chlorophenol. Separ. Purif. Technol. 292, 120984 https://doi.org/10.1016/j.seppur.2022.120984.

Aziz, F.F.A., Jalil, A.A., Triwahyono, S., Mohamed, M., 2018. Controllable structure of fibrous SiO_2–ZSM-5 support decorated with TiO_2 catalysts for enhanced photodegradation of paracetamol. Appl. Surf. Sci. 455, 84–95. https://doi.org/10.1016/j.apsusc.2018.05.183.

Aziz, F.F.A., Jalil, A.A., Hassan, N.S., Fauzi, A.A., Azami, M.S., 2021a. Simultaneous photocatalytic reduction of hexavalent chromium and oxidation of p-cresol over AgO decorated on fibrous silica zirconia. Environ. Pollut. 285, 117490 https://doi.org/10.1016/j.envpol.2021.117490.

Aziz, F.F.A., Jalil, A.A., Hassan, N.S., Hitam, C.N.C., Rahman, A.F.A., Fauzi, A.A., 2021b. Enhanced visible-light driven multi-photoredox Cr(VI) and p-cresol by Si and Zr interplay in fibrous silica-zirconia. J. Hazard Mater. 401, 123277 https://doi.org/10.1016/j.jhazmat.2020.123277.

Baca, M., Wenelska, K., Mijowska, E., Kaleńczuk, R.J., Zielińska, B., 2020. Physicochemical and photocatalytic characterization of mesoporous carbon/titanium dioxide spheres. Diam. Relat. Mater. 101, 107551 https://doi.org/10.1016/J.DIAMOND.2019.107551.

Bahari, M.B, Mamat, C.R, Jalil, A.A, Shing, L.S, Hassan, N.S, Aziz, F.F.A, Alhassan, M, Nawawi, M.G.M, Kidam, K, Setiabudi, H.D, 2022. Enriching the methanol generation via CO_2 photoconversion over the cockscomb-like fibrous silica copper. Fuel 328. https://doi.org/10.1016/J.FUEL.2022.125257.

Bembibre, A., Benamara, M., Hjiri, M., Gómez, E., Alamri, H.R., Dhahri, R., Serra, A., 2022. Visible-light driven sonophotocatalytic removal of tetracycline using Ca-doped ZnO nanoparticles. Chem. Eng. J. 427, 132006 https://doi.org/10.1016/J.CEJ.2021.132006.

Berkani, M., Smaali, A., Kadmi, Y., Almomani, F., 2022. Photocatalytic degradation of Penicillin G in aqueous solutions : kinetic, degradation pathway, and microbioassays assessment. J. Hazard Mater. 421, 126719 https://doi.org/10.1016/j.jhazmat.2021.126719.

Cai, Z., Song, Y., Jin, X., Wang, C.C., Ji, H., Liu, W., Sun, X., 2021. Highly efficient AgBr/h-MoO_3 with charge separation tuning for photocatalytic degradation of trimethoprim: mechanism insight and toxicity assessment. Sci. Total Environ. 781, 146754 https://doi.org/10.1016/J.SCITOTENV.2021.146754.

Dai, D., Qiu, J., Zhang, L., Ma, H., Yao, J., 2022. Amino-functionalized Ti-metal-organic framework decorated BiOI sphere for simultaneous elimination of Cr(VI) and tetracycline. J. Colloid Interface Sci. 607, 933–941. https://doi.org/10.1016/j.jcis.2021.09.084.

di Cerbo, A., Pezzuto, F., Guidetti, G., Canello, S., Corsi, L., 2019. Tetracyclines: insights and updates of their use in human and animal pathology and their potential toxicity. Open Biochem. J. 13, 1–12. https://doi.org/10.2174/1874091X01913010001.

Fatah, N.A.A., Jalil, A.A., Triwahyono, S., Yusof, N., Mamat, C.R., Izan, S.M., Hamid, M.Y.S., Hussain, I., Adnan, R.H., Abdullah, T.A.T., Nabgan, W., 2020. Favored hydrogenation of linear carbon monoxide over cobalt loaded on fibrous silica KCC-1. Int. J. Hydrogen Energy 45, 9522–9534. https://doi.org/10.1016/j.ijhydene.2020.01.144.

Fauzi, A.A., Jalil, A.A., Mohamed, M., Triwahyono, S., Jusoh, N.W.C., Rahman, A.F.A., Aziz, F.F.A., Hassan, N.S., Khusnun, N.F., Tanaka, H., 2018. Altering fiber density of cockscomb-like fibrous silica–titania catalysts for enhanced photodegradation of ibuprofen. J. Environ. Manag. 227, 34–43. https://doi.org/10.1016/j.jenvman.2018.08.073.

Fauzi, A.A., Jalil, A.A., Hitam, C.N.C., Aziz, F.F.A., Chanlek, N., 2020a. Superior sulfate radicals-induced visible-light-driven photodegradation of pharmaceuticals by appropriate Ce loading on fibrous silica ceria. J. Environ. Chem. Eng. 8, 104484 https://doi.org/10.1016/j.jece.2020.104484.

Fauzi, A.A., Jalil, A.A., Mohamed, M., Naseri, N.A., Hitam, C.N.C., Khusnun, N.F., Hassan, N.S., Rahman, A.F.A., Aziz, F.F.A., Azmi, M.S.M., 2020b. Fibrous silica induced narrow band gap TiO_2 catalyst for enhanced visible light-driven photodegradation of methylene blue. In: IOP Conf. Ser. Mater. Sci. Eng., vol. 808. https://doi.org/10.1088/1757-899X/808/1/012016, 0–10.

Fauzi, A.A., Jalil, A.A., Hassan, N.S., Aziz, F.F.A., Azami, M.S., Abdullah, T.A.T., Kamaroddin, M.F.A., Setiabudi, H.D., 2022. An intriguing Z-scheme titania loaded on fibrous silica ceria for accelerated visible-light-driven photocatalytic degradation of ciprofloxacin. Environ. Res. 211, 113069 https://doi.org/10.1016/J.ENVRES.2022.113069.

Fu, L., Chen, H., Wang, K., Wang, X., 2022. Oxygen-vacancy generation in $MgFe_2O_4$ by high temperature calcination and its improved photocatalytic activity for CO_2 reduction. J. Alloys Compd. 891, 161925 https://doi.org/10.1016/J.JALLCOM.2021.161925.

Girish, C.R., 2020. Removal of heavy metals from pharmaceutical wastewater by adsorption using agricultural waste: a review. Int. J. Pharmacol. Res. 12, 228–236. https://doi.org/10.31838/IJPR/2020.12.04.038.

Guo, H., Niu, C.G., Zhang, L., Wen, X.J., Liang, C., Zhang, X.G., Guan, D.L., Tang, N., Zeng, G.M., 2018. Construction of direct Z-Scheme $AgI/Bi_2Sn_2O_7$ nanojunction system with enhanced photocatalytic activity: accelerated interfacial charge transfer induced efficient Cr(VI) reduction, tetracycline degradation and escherichia coli inactivation. ACS Sustain. Chem. Eng. 6, 8003–8018 https://doi.org/10.1021/acssuschemeng.8b01448.

Hassan, N.S, Jalil, A.A, Azami, M.S, Rahman, A.F.A, Firmansyah, M.L, Nabgan, W, 2021. Photodegradation of bisphenol A from aqueous solution over reduced graphene oxide supported on tetragonal silica-zirconia nanocatalysts: optimization using RSM. Process Saf. Environ. Prot. 156, 496–507. https://doi.org/10.1016/J.PSEP.2021.10.032.

Hassan, N.S, Jalil, A.A, Hitam, C.N.C, Sawal, M.H, Rahim, M.N.S, Hussain, I, Jusoh, N.W.C, Saravanan, R, Prasetyoko, D, 2022. Enhanced photooxidative desulphurization of dibenzothiophene over fibrous silica tantalum: Influence of metal-disturbance electronic band structure. Int. J. Hydrogen Energy. https://doi.org/10.1016/J.IJHYDENE.2022.02.008. In press.

Hassan, N.S., Jalil, A.A., Satar, M.A.H., Hitam, C.N.C., Aziz, F.F.A., Fauzi, A.A., Aziz, M.A.A., H, B., 2020. Novel fabrication of photoactive CuO/HY zeolite as an efficient catalyst for photodecolorization of Malachite Green. Top. Catal. 63, 1005–1016. https://doi.org/10.1007/s11244-020-01314-y.

Heidarpour, H., Padervand, M., Soltanieh, M., Vossoughi, M., 2020. Enhanced decolorization of Rhodamine B solution through simultaneous photocatalysis and persulfate activation over Fe/C_3N_4 photocatalyst. Chem. Eng. Res. Des. 153, 709–720. https://doi.org/10.1016/J.CHERD.2019.09.007.

Hemmati-Eslamlu, P., Habibi-Yangjeh, A., Asadzadeh-Khaneghah, S., Chand, H., Krishnan, V., 2021. Integration g-C_3N_4 nanotubes and Sb_2MoO_6 nanoparticles: impressive photoactivity for tetracycline degradation, Cr(VI) reduction, and organic dyes removals under visible light. Adv. Powder Technol. 32, 2322–2335. https://doi.org/10.1016/j.apt.2021.05.007.

Hitam, C.N.C, Jalil, A.A, Izan, S.M, Azami, M.S, Hassim, M.H, Chanlek, N, 2020a. The unforeseen relationship of Fe_2O_3 and ZnO on fibrous silica KCC-1 catalyst for fabricated Z-scheme extractive-photooxidative desulphurization. Powder Technol. 375, 397–408. https://doi.org/10.1016/j.powtec.2020.07.114.

Hitam, C.N.C., Jalil, A.A., Raji, Y.O., 2020b. Fabrication of fibrous silica zinc (FSZn) composite for enhanced photocatalytic desulphurization. Top. Catal. 63, 1169–1181. https://doi.org/10.1007/S11244-020-01275-2/FIGURES/10.

Hojabri, A., Hajakbari, F., Meibodi, A.E., 2015. Structural and optical properties of nanocrystalline α-MoO3 thin films prepared at different annealing temperatures. J. Theor. Appl. Phys. 9, 67–73. https://doi.org/10.1007/s40094-014-0161-5.

Hu, H., Deng, C., Xu, J., Zhang, K., Sun, M., 2015. Metastable h-MoO_3 and stable α-MoO_3 microstructures: controllable synthesis, growth mechanism and their enhanced photocatalytic activity. J. Exp. Nanosci. 10, 1336–1346. https://doi.org/10.1080/17458080.2015.1012654.

Izzudin, N.M., Jalil, A.A., Aziz, F.F.A., Azami, M.S., Ali, M.W., Hassan, N.S., Rahman, A.F.A., Fauzi, A.A., Vo, D.V.N., 2021. Simultaneous remediation of hexavalent chromium and organic pollutants in wastewater using period 4 transition metal oxide-based photocatalysts: a review. Environ. Chem. Lett. 196 19, 4489–4517. https://doi.org/10.1007/S10311-021-01272-1, 2021.

Jannat Abadi, M.H., Nouri, S.M.M., Zhiani, R., Heydarzadeh, H.D., Motavalizadehkakhky, A., 2019. Removal of tetracycline from aqueous solution using Fe-doped zeolite. Int. J. Ind. Chem. 10, 291–300. https://doi.org/10.1007/S40090-019-0191-6/FIGURES/10.

Jiang, L., Xie, Y., He, F., Ling, Y., Zhao, J., Ye, H., Li, S., Wang, J., Hou, Y., 2021. Facile synthesis of GO as middle carrier modified flower-like BiOBr and C_3N_4 nanosheets for simultaneous treatment of chromium (VI) and tetracycline. Chin. Chem. Lett. 32, 2187–2191. https://doi.org/10.1016/j.cclet.2020.12.010.

Joya, M.R., Alfonso, J.E., Moreno, L.C., 2019. Photoluminescence and Raman studies of α-MoO3 doped with erbium and neodymium. Curr. Sci. 116, 1690–1695. https://doi.org/10.18520/cs/v116/i10/1690-1695.

Keerthana, S.P., Yuvakkumar, R., Senthil Kumar, P., Ravi, G., Hong, S.I., Velauthapillai, D., 2022. Investigation of pure and g-C_3N_4 loaded $CdWO_4$ photocatalytic activity on reducing toxic pollutants. Chemosphere 291, 133090. https://doi.org/10.1016/j.chemosphere.2021.133090.

Kumar, K.V.A., Lakshminarayana, B., Suryakala, D., Subrahmanyam, C., 2020. Reduced graphene oxide supported ZnO quantum dots for visible light-induced simultaneous removal of tetracycline and hexavalent chromium. RSC Adv. 10, 20494–20503. https://doi.org/10.1039/d0ra02062a.

Li, W., Chen, J., Guo, R., Wu, J., Zhou, X., Luo, J., 2017. Facile fabrication of a direct Z-scheme MoO₃/Ag₂CrO₄ composite photocatalyst with improved visible light photocatalytic performance. J. Mater. Sci. Mater. Electron. 28, 15967–15979. https://doi.org/10.1007/s10854-017-7495-0.

Li, C., Zhao, Z., Fu, S., Wang, X., Ma, Y., Dong, S., 2021. Polyvinylpyrrolidone in the one-step synthesis of carbon quantum dots anchored hollow microsphere Bi₂WO₆ enhances the simultaneous photocatalytic removal of tetracycline and Cr (VI). Separ. Purif. Technol. 270, 118844 https://doi.org/10.1016/j.seppur.2021.118844.

Li, Q.H., Dong, M., Li, R., Cui, Y.Q., Xie, G.X., Wang, X.X., Long, Y.Z., 2021. Enhancement of Cr(VI) removal efficiency via adsorption/photocatalysis synergy using electrospun chitosan/g-C₃N₄/TiO₂ nanofibers. Carbohydr. Polym. 253, 117200 https://doi.org/10.1016/J.CARBPOL.2020.117200.

Liu, Q., Wu, Y., Zhang, J., Chen, K., Huang, C., Chen, H., Qiu, X., 2019. Plasmonic MoO₃-x nanosheets with tunable oxygen vacancies as efficient visible light responsive photocatalyst. Appl. Surf. Sci. 490, 395–402. https://doi.org/10.1016/j.apsusc.2019.06.099.

Liu, G., Abukhadra, M.R., El-Sherbeeny, A.M., Mostafa, A.M., Elmeligy, M.A., 2020. Insight into the photocatalytic properties of diatomite@Ni/NiO composite for effective photo-reduction of malachite green dye and photo-reduction of Cr (VI) under visible light. J. Environ. Manag. 254 https://doi.org/10.1016/j.jenvman.2019.109799.

Liu, Lishuo, Huang, J., Yu, H., Wan, J., Liu, Lianyu, Yi, K., Zhang, W., Zhang, C., 2021a. Construction of MoO₃ nanopaticles/g-C₃N₄ nanosheets 0D/2D heterojuntion photocatalysts for enhanced photocatalytic degradation of antibiotic pollutant. Chemosphere 282, 131049. https://doi.org/10.1016/J.CHEMOSPHERE.2021.131049.

Liu, Lishuo, Huang, J., Yu, H., Wan, J., Liu, Lianyu, Yi, K., Zhang, W., Zhang, C., 2021b. Construction of MoO₃ nanopaticles/g-C₃N₄ nanosheets 0D/2D heterojuntion photocatalysts for enhanced photocatalytic degradation of antibiotic pollutant. Chemosphere 282, 131049. https://doi.org/10.1016/j.chemosphere.2021.131049.

Ma, Z., Jia, Q., Shi, Y., Duan, X., Han, B., 2020. Synergistic effect of aeration-assisted photocatalysis: two parallel mechanism pathways for TXP-10 surfactant removal. J. Water Proc. Eng. 38, 101618 https://doi.org/10.1016/j.jwpe.2020.101618.

Mafa, P.J., Swana, U.S., Liu, D., Gui, J., Mamba, B.B., Kuvarega, A.T., 2021. Synthesis of Bi₅O₇I-MoO₃ photocatalyst via simultaneous calcination of BiOI and MoS₂ for visible light degradation of ibuprofen. Colloids Surfaces A Physicochem. Eng. Asp. 612, 126004 https://doi.org/10.1016/J.COLSURFA.2020.126004.

Oluwole, A.O., Olatunji, O.S., 2022. Photocatalytic degradation of tetracycline in aqueous systems under visible light irridiation using needle-like SnO₂ nanoparticles anchored on exfoliated g-C₃N₄. Environ. Sci. Eur. 34, 1–14. https://doi.org/10.1186/S12302-021-00588-7/TABLES/2.

Ouyang, C., Quan, X., Zhang, C., Pan, Y., Li, X., Hong, Z., Zhi, M., 2021. Direct Z-scheme ZnIn₂S₄@MoO₃ heterojunction for efficient photodegradation of tetracycline hydrochloride under visible light irradiation. Chem. Eng. J. 424, 130510 https://doi.org/10.1016/j.cej.2021.130510.

Prakash, N.G., Dhananjaya, M., Narayana, A.L., Maseed, H., Srikanth, V.V.S.S., Hussain, O.M., 2019. Improved electrochemical performance of rGO-wrapped MoO₃ nanocomposite for supercapacitors. Appl. Phys. Mater. Sci. Process 125, 1–10. https://doi.org/10.1007/s00339-019-2779-2.

Reddy, C.V., Koutavarapu, R., Shim, J., Cheolho, B., Reddy, K.R., 2022. Novel g-C3N4/Cu-doped ZrO₂ hybrid heterostructures for efficient photocatalytic Cr(VI) photoreduction and electrochemical energy storage applications. Chemosphere 295. https://doi.org/10.1016/j.chemosphere.2022.133851.

Seid, L., Lakhdari, D., Berkani, M., Belgherbi, O., Chouder, D., Vasseghian, Y., Lakhdari, N., Proc, D., 2022. High-efficiency electrochemical degradation of phenol in aqueous solutions using Ni-PPy and Cu-PPy composite materials. J. Hazard Mater. 423, 126986 https://doi.org/10.1016/j.jhazmat.2021.126986.

Shahul Hamid, M.Y., Triwahyono, S., Jalil, A.A., Che Jusoh, N.W., Izan, S.M., Tuan Abdullah, T.A., 2018. Tailoring the properties of metal oxide loaded/KCC-1 toward a different mechanism of CO₂ Methanation in situ IR and ESR. Inorg. Chem. 57, 5859–5869. https://doi.org/10.1021/acs.inorgchem.8b00241.

Shahul Hamid, M.Y., Abdul Jalil, A., Abdul Rahman, A.F., Tuan Abdullah, T.A., 2019. Enhanced reactive CO₂ species formation: via V₂O₅-promoted Ni/KCC-1 for low temperature activation of CO₂ methanation. React. Chem. Eng. 4, 1126–1135. https://doi.org/10.1039/c8re00312b.

Song, N., Zhang, S., Zhong, S., Su, X., Ma, C., 2022. A direct Z-scheme polypyrrole/Bi₂WO₆ nanoparticles with boosted photogenerated charge separation for photocatalytic reduction of Cr(VI): characteristics, performance, and mechanisms. J. Clean. Prod. 337, 130577 https://doi.org/10.1016/J.JCLEPRO.2022.130577.

Tahmasebi, N., Esmaeilpour, H., Movahedifard, F., Hakimyfard, A., Moayeri, H., 2021. Fabrication of a novel MoO₃/Cs₃PMo₁₂O₄₀ composite for photocatalytic decolorization of rhodamine B. Mater. Sci. Semicond. Process. 131, 105876 https://doi.org/10.1016/j.mssp.2021.105876.

Valério, A., Wang, J., Tong, S., Ulson de Souza, A.A., Hotza, D., Gómez González, S.Y., 2020. Synergetic effect of photocatalysis and ozonation for enhanced photocatalytic degradation using highly macroporous photocatalytic supports. Chem. Eng. Process. - Process Intensif. 149, 107838 https://doi.org/10.1016/J.CEP.2020.107838.

Wan, J., Zhang, Y., Wang, R., Liu, L., Liu, E., Fan, J., Fu, F., 2020. Effective charge kinetics steering in surface plasmons coupled two-dimensional chemical Au/Bi₂WO₆-MoS₂ heterojunction for superior photocatalytic detoxification performance. J. Hazard Mater. 384 https://doi.org/10.1016/j.jhazmat.2019.121484.

Wang, J., Lei, X., Huang, C., Xue, L., Cheng, W., Wu, Q., 2021. Fabrication of a novel MoO3/Zn–Al LDHs composite photocatalyst for efficient degradation of tetracycline under visible light irradiation. J. Phys. Chem. Solid. 148 https://doi.org/10.1016/j.jpcs.2020.109698.

Wei, W., Zhang, Z., You, G., Shan, Y., Xu, Z., 2019. Preparation of recyclable MoO₃ nanosheets for visible-light driven photocatalytic reduction of Cr(VI). RSC Adv. 9, 28768–28774. https://doi.org/10.1039/C9RA05644K.

Xiao, J., Lv, J., Lu, Q., 2022. Building Fe₂O₃/MoO₃ nanorod heterojunction enables better tetracycline photocatalysis. Mater. Lett. 311, 131580 https://doi.org/10.1016/J.MATLET.2021.131580.

Yaashikaa, P.R., Kumar, P.S., 2022. Fabrication and characterization of magnetic nanomaterials for the removal of toxic pollutants from water environment: a review. Chemosphere 303, 135067. https://doi.org/10.1016/j.chemosphere.2022.135067.

Yan, Y., Ma, C., Huang, H., Yu, K., Liu, Y., Li, C., Zhu, Z., Huo, P., Tang, X., Liu, Y., Lu, Z., 2020. A 2D mesoporous photocatalyst constructed by the modification of biochar on BiOCl ultrathin nanosheets for enhancing the TC-HCl degradation activity. New J. Chem. 44, 79–86. https://doi.org/10.1039/c9nj05219d.

Yang, Q., Bao, X., Li, Z., Yang, A., Cao, Y., Hu, X., Yu, L., Liu, B., 2022. Visible-light-enhanced Cr (VI) reduction at MXene photocathode in photoelectrocatalytic microbial fuel cells. J. Water Proc. Eng. 45, 102454 https://doi.org/10.1016/j.jwpe.2021.102454.

Ye, J., Liu, J., Huang, Z., Wu, S., Dai, X., Zhang, L., Cui, L., 2019. Effect of reduced graphene oxide doping on photocatalytic reduction of Cr(VI) and photocatalytic oxidation of tetracycline by ZnAlTi layered double oxides under visible light. Chemosphere 227, 505–513. https://doi.org/10.1016/j.chemosphere.2019.04.086.

Zdarta, J., Jesionowski, T., Meyer, A.S., Pinelo, M., 2022. Removal of tetracycline in enzymatic membrane reactor: enzymatic conversion as the predominant mechanism over adsorption and membrane rejection. J. Environ. Chem. Eng. 10, 106973 https://doi.org/10.1016/J.JECE.2021.106973.

Zhang, Q., Wang, M., Ao, M., Luo, Y., Zhang, A., Zhao, L., Yan, L., Deng, F., Luo, X., 2019. Solvothermal synthesis of Z-scheme AgIn₅S₈/Bi₂WO₆ nano-heterojunction with excellent performance for photocatalytic degradation and Cr(VI) reduction. J. Alloys Compd. 805, 41–49. https://doi.org/10.1016/j.jallcom.2019.06.331.

Zhang, Q., Xu, Jun, Ma, X., Xu, Jinmei, Yun, Z., Zuo, Q., Wang, L., 2021. A novel Fe-based bi-MOFs material for photocatalytic degradation of tetracycline: performance, mechanism and toxicity assessment. J. Water Proc. Eng. 44, 102364 https://doi.org/10.1016/j.jwpe.2021.102364.

Zhang, J., Ma, Y., Zhang, W., Huang, X., Wang, X., Huang, Y., Zhang, P., 2022. CuBi2O4/calcined ZnAlBi-LDHs heterojunction: simultaneous removal of Cr(VI) and tetracycline through effective adsorption and photocatalytic redox. J. Clean. Prod. 365, 132810 https://doi.org/10.1016/J.JCLEPRO.2022.132810.

Zhao, W., Li, J., Dai, B., Cheng, Z., Xu, J., Ma, K., Zhang, L., Sheng, N., Mao, G., Wu, H., Wei, K., Leung, D.Y.C., 2019. Simultaneous removal of tetracycline and Cr(VI) by a novel three-dimensional AgI/BiVO₄ p-n junction photocatalyst and insight into the photocatalytic mechanism. Chem. Eng. J. 369, 716–725. https://doi.org/10.1016/J.CEJ.2019.03.115.

Zhou, Y., Zhang, C., Huang, D., Wang, W., Zhai, Y., Liang, Q., Yang, Y., Tian, S., Luo, H., Qin, D., 2022. Structure defined 2D Mo₂C/2Dg-C₃N₄ Van der Waals heterojunction: oriented charge flow in-plane and separation within the interface to collectively promote photocatalytic degradation of pharmaceutical and personal care products. Appl. Catal. B Environ. 301, 120749 https://doi.org/10.1016/j.apcatb.2021.120749.